Planetary and Space Science 204 (2021) 105251

Contents lists available at ScienceDirect

Planetary and Space Science

journal homepage: www.elsevier.com/locate/pss

The chemical composition and homogeneity of the Allende matrix

M.B. Neuland [a,*,1], K. Mezger [b], A. Riedo [a], M. Tulej [a], P. Wurz [a,**]

[a] University of Bern, Physics Institute, Space Research and Planetary Sciences, Sidlerstrasse 5, CH – 3012, Bern, Switzerland
[b] University of Bern, Institute of Geological Sciences, Baltzerstrasse 3, CH – 3012, Bern, Switzerland

ARTICLE INFO

Keywords:
Chondrite matrix element abundances
Solar system condensation sequence
Fs – LIMS

ABSTRACT

The abundances of C, O, S, Na, K, Li, Mn, P, Cr, Si, Fe, Mg, Ni, Co, V, Ca, Ti, Al and Sc were determined in-situ in a sample of the Allende meteorite using a laser ablation/ionization mass spectrometer to quantify the bulk chemical composition of the matrix and its spatial chemical variability.

The high lateral resolution of the instrument makes it possible to measure the elemental composition of Allende matrix, without any sample treatment prior to analysis. The measurements of solely Allende matrix allow investigating the variability of the element abundances in the matrix material on different scales from 50 μm to 0.5 mm.

The comprehensive data set provides constraints on models for the formation of matrix material of carbonaceous chondrites in the solar nebula. A key observation of this study is a high degree of chemical homogeneity of the matrix, indicating that it formed independently from or in parallel with the chondrules and that the process that led to the formation of the parent body was a fast collapse of the dust-gas cloud following chondrule formation.

1. Introduction

Carbonaceous chondrites preserve closely the bulk composition of the solar nebula. Of all known materials, the chemical composition of chondrites, particularly CI, is closest to the chemical composition of the Sun, e.g., (McSween and Richardson, 1977). Among the different carbonaceous chondrites, Allende (CV3) is one of the best studied meteorites, because of the large mass of material recovered (Clarke et al., 1971). Allende chondrules and refractory calcium-aluminum-rich inclusions (CAI), for example, have been studied extensively to reconstruct the nucleosynthetic origin of the components, the physical and chemical conditions during their accretion, and the corresponding time scale of these early solar system processes (e.g., Wark, 1979; Brearley, 1999; Amelin et al., 2002; MacPherson and Boss, 2011; Jacquet et al., 2015). Such analyses include determination of the chemical and isotopic composition, as well as studies of the mineralogy and petrology of CAIs, chondrules and matrix. Considering the different components of Allende, the matrix is the least studied. Among all meteorite components the matrices of the most primitive carbonaceous chondrites are thought to be mostly unaltered (McSween and Richardson, 1977; Buseck and Hua, 1993). Most probably, the reason for the comparably poor attention given to chondrite matrix is that classical methods for the investigation of meteorites require efficient and clean separation of the matrix material from other components. However, it is challenging to separate the different components quantitatively from the matrix using mechanical methods. Thus, obtaining a sample that represents pure matrix material is complicated and difficult (Jarosewich, 1990).

In the present study we used in situ laser ablation/ionization mass spectrometry (LIMS) for the measurements, which does not require any sample treatment, contrary to many other methods for chemical composition analysis. The instrument, named “LMS” in the following, was designed and purpose-built for in-situ measurements of rocks and soils on a planetary lander or rover for a space research mission. The narrow laser focus allows chemical composition measurements with high spatial resolution (laser spot size of approximately 10 μm) in selected regions of interest. This minimizes cross contamination of the component of interest by other components of the sample and minimizes sample consumption, particularly for laboratory experiments. Other in-situ

* Corresponding author.
** Corresponding author.
E-mail addresses: maike.neuland@dlr.de (M.B. Neuland), peter.wurz@space.unibe.ch (P. Wurz).
[1] Present address: German Aerospace Centre (DLR) Lampoldshausen, Institute of Technical Physics, Atmospheric Propagation and Effect, D - 74 239, Hardthausen, Germany.

https://doi.org/10.1016/j.pss.2021.105251
Received 2 January 2021; Received in revised form 25 March 2021; Accepted 11 May 2021
Available online 18 May 2021

methods, electron microprobe analysis (EPMA) for example, have been used to study meteorite matrix material, but the method is subject to matrix effects, and the abundance of most trace elements (abundances in low ppm to ppb range) cannot be detected with high accuracy and precision. In addition, the beam size usually too large to study specific meteorite components, except for field-emission EPMA. Transmission electron microscopy can be used to study μm thin slices of the sample of interest. However these analyses are very time-consuming, which makes it impossible to study large sample areas (Abreu and Brearley, 2010). Other techniques that are commonly used for chemical composition measurements include X-ray fluorescence, or neutron activation measurements. However, compared to LIMS, these methods generally require very long data acquisition times (hours to several days), and several mg of sample material. For the analysis of the Allende meteorite with the LMS we used a femtosecond laser operated with a repetition rate of 1 kHz. The fast completion of measurements not only reduces the time for data acquisition without compromising data quality, but assures unchanged measurement conditions during the collection of large amounts of data. The LMS resolution and sensitivity, although lower than for example those of secondary electron microscopy (SEM), are adequate to obtain scientifically highly valuable concentration data for a large spectrum of elements.

Hypotheses for the chemical evolution and condensation of the solar nebula have been constrained for example by intense studies of CAIs (Wänke et al., 1974). The high abundance of refractory elements in the CAIs led to the theory that these components were most probably the first solids that condensed from the early solar nebula. Chondrules, which formed from high-temperature melts, are an important and characteristic component of primitive meteorites, but the nature of the processes that formed them remains a subject of discussion (e.g., Wark, 1979; Morfill et al., 1998; Stracke et al., 2012; Alexander, 2005; Alexander and Ebel, 2012; Jones, 2012; Friend et al., 2016; Olsen et al., 2016; Schrader et al., 2018; Desch et al., 2012). However, numerous studies have shown that the chondrules are chemically complementary to the matrix material, which is richer in the more volatile elements (Palme et al., 2015). A possible explanation for the different concentrations of volatile and refractory elements in individual meteorite components could be that the components formed from different reservoirs of the solar nebula and possibly at different times.

The chemical composition of the matrix of carbonaceous chondrites could contain valuable information needed to advance and refine existing models of formation and evolution of meteorites and their components, and thus of solar nebula condensation, and the formation of the first solids in the early Solar System.

2. Technique and measurements

2.1. Allende sample

We measured the chemical composition of the Allende matrix with a laser ablation/ionization mass spectrometer. This instrument has been designed and built at the University of Bern, Switzerland. The miniature LMS is highly compact (16 cm × 6 cm × 6 cm), light-weight and has low power consumption for the purpose of space exploration with the ultimate goal of operating the instrument on a rover or lander on a planetary surface for in situ chemical composition measurements of rocks and soil (Wurz et al., 2021). The sample is placed in the focus of the laser beam (19.9 TW/cm^2 in this study), and atoms are ablated and ionized from a spot with a diameter of about (12 ± 2) μm from the sample surface. A micro channel plate detector is used for the time-of-flight measurement. An example of a mass spectrum measured on the Allende meteorite is provided in appendix A, Figure A1. Details on the LMS, its design, operation and performance can be found in, e.g., Rohner et al. (2003), Riedo et al. (2013a, 2013b, 2013c, 2017), Tulej et al. (2012, 2014, 2015).

The Allende sample (10 mm × 10 mm × 5 mm) used in this study was introduced already in earlier reports (Neuland et al., 2014). The sample contains a variety of small chondrules and CAIs. An image of the sample surface as a whole can be found in Neuland et al. (2014). For the measurements presented here, an approximately 200 μm thick layer was cut off from the surface with a diamond saw blade to remove the ablation craters of the previous measurements. Otherwise, no additional treatment, neither mechanical nor chemical, was applied to the sample.

Fig. 1 shows a detail of the sample surface with the regions of interest that were selected for this study. These regions include the areas M1, M2 and M3 that contain only matrix, and areas X1 and X2 that contain chondrules, CAIs and matrix.

2.2. Data sampling and selection

Fig. 2 shows the areas M1 (a), M2 (b) and M3 (c) before (left panels) and after (right panels) the LMS measurements. On very small scales (few μm) the matrix contains pure minerals and metals and often it is not possible to evaluate from the optical images if isolated mineral grains are genuine matrix material or chondrule fragments (Tanaka and Akai, 1997; Frank et al., 2014). In this study 60′000 laser pulses were applied in each single position on the sample. The diameter of the laser ablation craters was constant, and the analyzed area was about (12 ± 2) μm in diameter for all single measurement spots on Allende. In principle, the instrument would allow distances between the measurement points as small as the crater diameter and less. However, the sampling distance in both horizontal directions was set larger than that to minimize the risk of cross-contamination between individual measurements. For the areas M1– M3 a sampling distance of 50 μm was chosen, representing the lateral resolution of the measurements. As the grain size of Allende matrix components is in the μm to sub-μm range (Toriumi, 1989; Zolensky et al., 1993), the spatial resolutio n of the measurements is not sufficient to resolve the chemical composition of individual matrix grains directly. However, the high sensitivity and dynamic range of the LMS instrument allow quantitative measurements of differences in chemical composition down to the level of tens of ppb for adjacent measurement positions.

The matrix also contains grains that may not be part of the genuine matrix material. An example is shown in the optical image of area M2 (Fig. 2b) as a dark spot with a diameter of about 120 μm (marked by a white arrow). High abundances of Ca, Al and Fe in the corresponding measurements are a sign for a dark inclusion. By careful investigation of

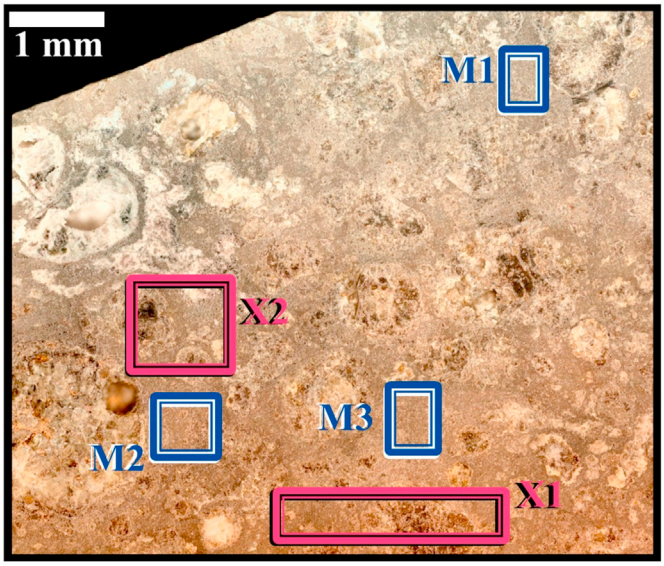

Fig. 1. Allende sample.
The optical image shows the different regions of interest that were selected on the sample of Allende meteorite, three areas M1 – M3 on the meteorite matrix, and two areas X1 and X2, which include a variety of chondrules and CAIs, and matrix material.

	Area	Number of measurement points (pattern)
a)	*M1*	*154 (11 x 14)*
b)	*M2*	*272 (17 x 16)*
c)	*M3*	*238 (14 x 17)*
		664 analyses total, 609 identified as matrix

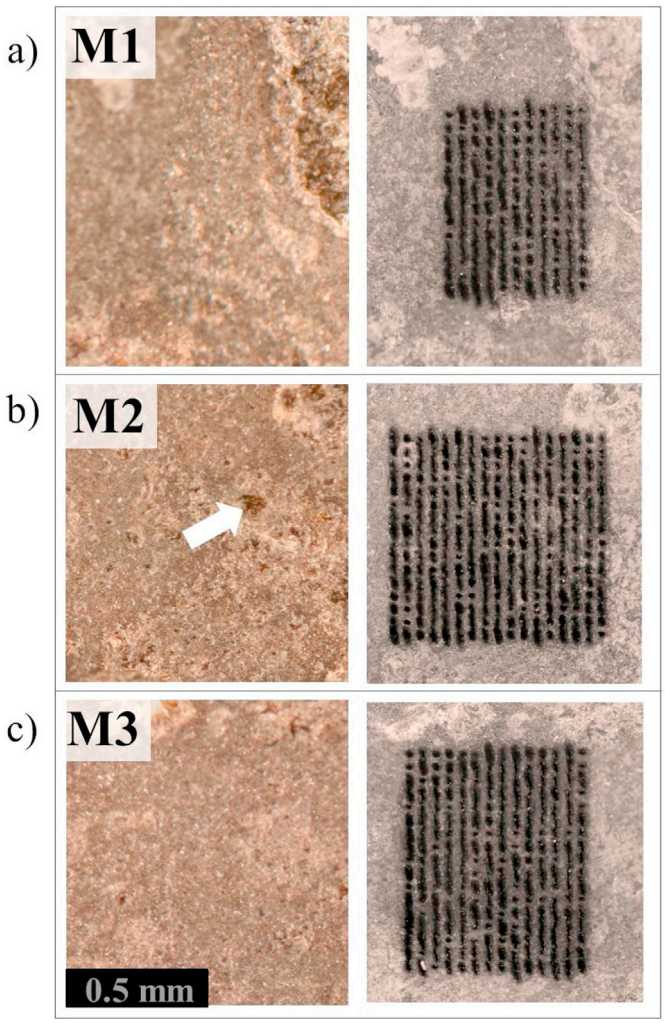

Fig. 2. *Matrix measurements*. Details of the regions of interest on the meteorite matrix M1 – M3 (compare Fig. 1) before (left column) and after (right column) the LMS measurements. The white arrow in b) points to a spot that is questionable to be matrix material. The figure scale is the same for a), b) and c).

the optical images of the areas M1 – M3 and the analyses of the corresponding mass spectra, in total 55 measurement positions were identified to have largely differing element abundances compared to all matrix measurements.

The capabilities of the LMS instrument allow identification of such individual positions that have a very different chemical composition. This identification constitutes a base for composing a representative data set, because the data set can be tested with different thresholds for including/excluding individual positions and thus, making the data selection transparent and reproducible. In case of Allende matrix, all analyses deviating more than 5 σ from the mean of all measurements of the corresponding element in areas M1 – M3 were excluded. In particular, in all these 55 positions the abundance of either S, Fe or Ni was decisive for excluding the measurement from the matrix analyses. Therefore, the areas M1 – M3 give a set of 664 measurements of which 609 measurements are of Allende matrix.

In Fig. 3 the two regions of interest X1 and X2 before and after the LMS measurements are shown. The spacing between the individual measurement positions was set to 50 μm for area X1 and to 100 μm for area X2. Riedo et al. (2016), Fig. 3 therein, showed that the sharp boundaries between matrix and chondrules in Allende are clearly visible in element maps composed from the LMS measurements, given that elements that have different abundances in the different components, are surveyed. As an example, the element maps of Al, Si and Fe for the area X1 are included in Appendix A, Figure A2. Such maps complement the optical images, and allow distinguishing between different components of the sample on small scales. In some cases, the chemical composition of similarly looking material might differ. The opposite was also observed, where materials that appeared very different in the optical image showed similar abundance of some elements. Optical images combined with maps of Si, Mg, Fe, C and S in particular allow identifying locations of matrix material inside the areas X1 and X2. This resulted in 296 matrix measurements for X1, and in 107 matrix for X2. A similar procedure of data selection was described and justified in Watt et al. (2006). Obtaining a sample that is representative for the specific analysis often constitutes a problem, and will always introduce a bias of the experimentalist, as also mentioned in, e.g., McSween and Richardson (1977). However, the procedure of data selection used in this study certainly represents the best possible effort, because considering only one of the two indicators (optical images, as in many mechanical analysis techniques, or chemical composition) imposes a high risk of misinterpreting the chemical analyses.

In total, the measurements resulted in a comprehensive data set consisting of 1651 measurement positions (M1 – M3, X1 and X2). Out if these 1651 measurements 1012 (609 from M1 – M3, 403 from X1 and X2) were identified as matrix material, 639 measurements (55 from M1 – M3, 548 from X1 and X2) are non-matrix material. The complete data set consists of about 60% matrix and 40% other components (chondrules, CAIs, dark inclusions, metal phases), i.e., material that represents the coarse components of the Allende sample (Frank et al., 2914; Norton,

	Area	Number of measurements (pattern)	Number of measurements identified as matrix
a)	X1	819 (63 x 13)	296
b)	X2	168 (14 x 12)	107

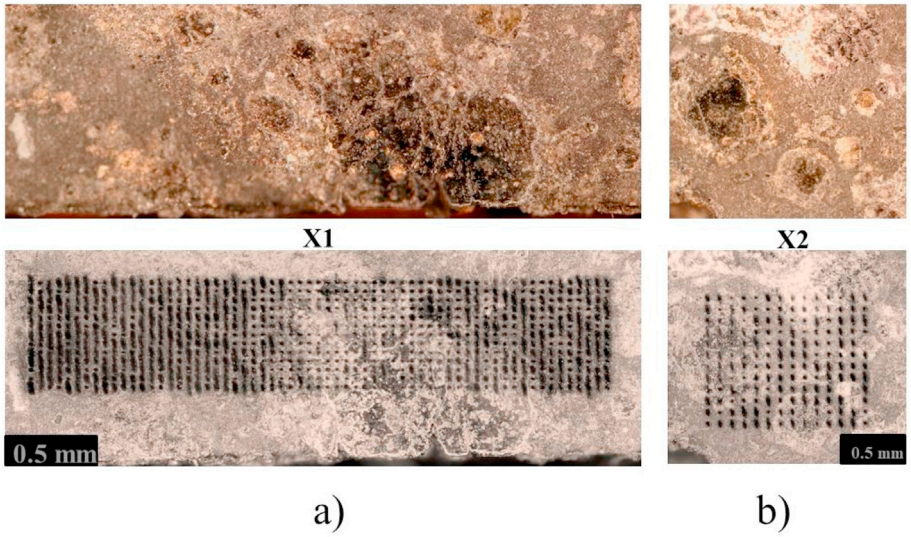

Fig. 3. Addendum to Allende bulk.
Images of details of the regions of interest X1 and X2 (compare to Fig. 1), containing various chondrules embedded in matrix.

2002). Similar results have been obtained for smaller samples of Allende (Simon et al., 2018). While consuming a very small sample amount (a few tens to hundreds of femto-grams of material), it can be stated that the LMS measurements can generate a representative data set for Allende bulk and matrix bulk compositions, because the sampling spots are well placed.

3. Method and data analysis

3.1. Element analysis

Data analysis was performed with an analysis software, that was specifically developed for time-of-flight instruments (Meyer et al., 2017). The conversion of signal intensities of individual isotopes to elements was carried out under the assumption of terrestrial isotope abundances (Becker, 2007). For details of the calculation see Neuland et al. (2014), Eq. 2. Only interference-free isotopes were used for the element abundance calculations, as listed in Table A1 in the appendix.

A large number of measurements was combined to derive a representative composition for the Allende matrix. Instead of taking the mean or median over all matrix or non-matrix measurements, the abundances of each element, individually derived from all matrix measurements, were binned into a histogram. The abundance of the corresponding element then is the expected value of the Gaussian fitted to this histogram, and the width of the fit directly gives the statistical scatter of the abundance. Investigation of the skewness and kurtosis of the Gauss fits additionally ensured the accuracy of the method. In addition, outliers, which were not cut off by the 5 σ threshold (Section 2.2), do not significantly affect the results in this method.

3.2. Quantitation and calibration

Similar to many analytical instruments, the sensitivity of a laser mass spectrometer is not the same for all elements. LIMS instruments are calibrated for quantitative analyses by deriving a set of relative sensitive coefficients (RSCs) for the elements of interest. An RSC equal to 1 defines the ideal case of the measured element abundance corresponding to the true element abundance. An RSC >1 specifies an overestimation of the abundance due to a higher sensitivity of the LMS to the corresponding element, which is the case, for example, for the alkali metals, which are readily ionized. Accordingly, an RSC <1 implies a lower sensitivity and thus an underestimation of the corresponding element. This is a well-established method, e.g. (Brinckerhoff et al., 2002; Li et al., 2010; Zhang et al., 2013; Sysoev et al., 2018), which becomes less error-prone by applying fs-laser irradiation, e.g. (Russo et al., 2002; Riedo et al., 2013a; Zhang et al., 2015). The uncertainties that result from correction of the element abundances by the according RSCs are smaller than the width of the distribution in all cases. A reliable calibration procedure has been developed and verified for the LMS at the University of Bern by measurements on different reference materials (Neuland et al., 2016). Using the RSCs derived in the studies presented in Neuland et al. (2016) was regarded as not being applicable for the investigation of Allende. Compared to the samples investigated earlier for deriving RSCs, the Allende sample exhibits a different porosity and a different chemical composition. Therefore, the laser irradiance, and consequently the voltage settings for the ion optical system and the detector had to be adjusted specifically to the sample, i.e. the instrument settings were systematically optimized to reach high sensitivity and mass resolution in the mass range selected for this study (~5 amu–65 amu). Additionally, due to the different composition, the experiment presented in Neuland et al. (2016) cannot provide RSCs for, e.g., C and Ni. However, except for the alkali metals, O, C, P and S all RSCs are close to 1, in agreement with the RSCs derived earlier (Neuland et al., 2016), at least for those elements included in both studies. The RSCs of the alkali metals are larger in this study, which is due to the combination of using a higher laser irradiance, necessary due to the harder sample, in combination with the very small ionization energies of these elements.

Similar to the procedure of earlier measurements on Allende with the ns-laser (Neuland et al., 2014), and because most literature reference values for Allende meteorite are available for the bulk composition, we selected regions of interest so that the measurements consist of 60% matrix material and 40% of other materials, according to the known

abundance of the different components in Allende (Clarke et al., 1971; Norton, 2002). As described in Section 2.2 this measurement set includes the three areas M1 – M3 on Allende matrix and additionally the two areas X1 and X2.

For the derivation of RSCs used in the analyses presented here, reference values for Allende bulk were taken from the study by Stracke et al. (2012), who present the abundances of a large number of elements determined with different techniques, suitably selected for specific major and trace elements of interest. However, this data set does not include element abundances for the alkali metals and C, S and Sc. Mason (1975) and Jarosewich (1990) also list abundances for these elements in bulk samples of Allende. The reported abundances of major elements in Allende bulk in these three publications are consistent. Although an Allende bulk sample was analyzed in all these analyses, such an agreement is not necessarily expected as different fragments of the meteorite were investigated. For this study reference values were taken primarily from Stracke et al. (2012), and also from Jarosewich (1990) and Mason (1975), when required. The reference values used for this study, and the resulting RSCs are given in appendix B (Figure B1Table B1).

3.3. Homogeneity analysis

The homogeneity of the matrix material was analyzed by applying a moving average filter to the measurement areas M1 – M3, a technique applied for example also in Morlok et al. (2006). The arithmetic average of the abundance of each element was calculated for different sizes of the moving grid, particularly for grids of 2 × 2, 3 × 3, 4 × 4, 5 × 5, 6 × 6 and 7 × 7 measurement positions. For a grid of size $p \times p$ applied to a measurement pattern of size $n \times m$ (compare caption of Fig. 2) the number of resulting averages is $(n - (p - 1)) \times (m - (p - 1))$. In Fig. 4 this is illustrated for a small example pattern of $n \times m = 4 \times 6$ measurement positions and how this is converted to a grid of abundance averages for one element. The first entry A_{11} contains the average from the measurement positions $nm = 11, 12, 21$ and 22, and the final grid of A has a size of 3 × 5. Subsequently, a grid of deviations σ was derived from the A - grid by subtracting the value that was determined by including all 1012 matrix measurements (see Section 2.2). The σ - grid has the same size as the A grid, and the units of the σ are the same as the unit of thecorresponding element abundance, e.g. ppm atomic fraction. For each grid size the resulting $\sigma's$ were plotted in a histogram. The widths of these distributions are a measure of the chemical homogeneity of the matrix on the spatial scale that corresponds to the number of analyses included, this is the area "sampling distance"-squared covered by the measurements of the moving grid. As an example, the histograms for vanadium (V) are shown in Fig. 5, where the upper panel "1 × 1" shows the deviation of the individual analyses (of M1 – M3) to the value determined from all 1012 measurement. In the sliding average analyses the matrix measurements from area X1 and X2 had to be excluded, because the regions contain chondrules at arbitrary locations in the grid. Pure matrix analyses in these two areas are spatially not as wide-spread as in the areas M1 – M3, which made it impossible to apply an automatic moving-average filter without including other materials, especially when applying grids larger than 2 × 2 measurement points. For keeping the analysis consistent, the 1 × 1 histograms contain only matrix analyses from areas M1 – M3 as well.

Because the abundance of V could be evaluated only from 607 of the matrix analyses the histogram of the 1 × 1 grid contains 607 entries accordingly, as noted by the number beside the grid size in the legend of Fig. 5. The number of histogram entries is decreasing with increasing grid size due to the limited number of total points available, based on the used method (Fig. 4). Additional examples of this analysis for Li, Si, and Sc are shown in Figure C1 in the appendix.

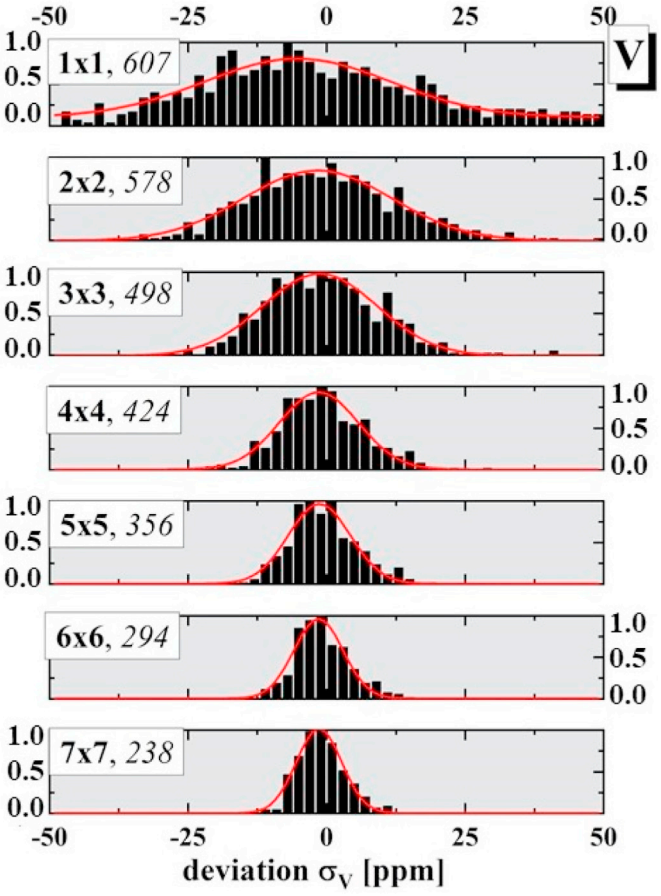

Fig. 5. Homogeneity analysis.
For each grid size of the moving average filter, the resulting deviations of the grid averages from the element abundance determined from all 1012 matrix analyses was plotted as a histogram, normalized to the maximum bin. The example shows all histograms for V analyses in the matrix areas M1 – M3.

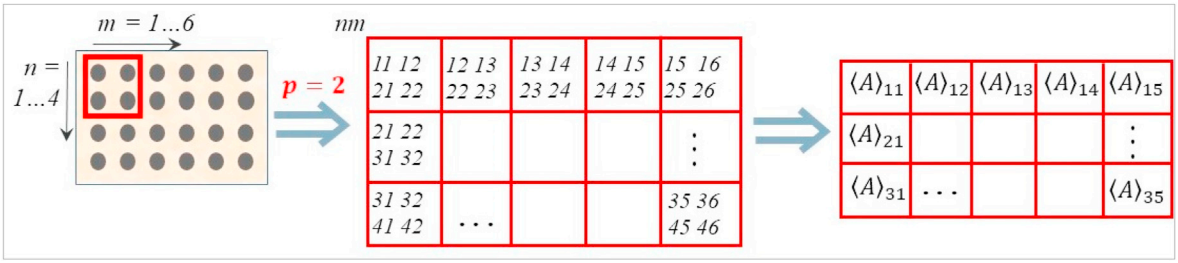

Fig. 4. Moving average.
This example shows how a grid of 3x5 average values is composed from a sliding average with grid size 2x2, thus p=2.

4. Results

4.1. Elemental composition

The results of elemental composition derived from all 1651 measurements are shown in the ternary plots in Fig. 6. The Si/(Mg + Fe) ratio (Fig. 6a) indicates an olivine-rich composition for the matrix with an additional component of Mg–Fe-rich minerals. The areas X1 and X2, which include chondrules and other components that contain minerals with a larger grain size than the matrix, have a large portion of olivine as well. In general, the two regions of interest X1 and X2 show higher Si/(Mg + Fe) than the matrix, and some individual Al-rich analyses.

The olivines in the Allende matrix have nearly equal amounts of forsterite and fayalite, with only a small shift towards Fe-rich olivine (Fig. 6b). The measured molar ratio of Fe/Mg is 1.28 ± 0.03, which agrees with previous studies, e.g. Wark (1979), where a ratio of FeO/MgO = 1.4 ± 0.1 is presented. A shift towards forsterite for the analyses in the areas X1 and X2 is clearly visible in Fig. 6b. Additionally, the non-matrix measurements contain minerals with higher contents of refractory elements, e.g., Al or Ca. Precisely, such data were found mostly along the rims of the larger chondrules in areas X1 and X2. A few measurements of X1 and X2 indicate a component of $Ca_3(Mg,Fe)_2$ as shown by the arrows along the corresponding ratios.

The C/Al/Na-ratios (Fig. 6c) show that the matrix of Allende meteorite contains C-rich material at some individual measurement positions. The other points can be identified as a mixture of melilite and albite. The ratios of (Na + Al)/Si, (K + Al)/Si and (Ca + Al)/Si (Fig. 6d) show that the matrix plagioclase has a higher albite component, while in areas X1 and X2 many analyses show essentially pure anorthite, attesting to the higher volatile element content in the matrix compared to the chondrules. The abundance of K-feldspar components is low.

Table 1 lists the element composition of Allende matrix normalized to the bulk composition. The matrix composition was derived from the areas M1 – M3 (total of 609 analyses) plus the individual measurements from areas X1 and X2 that were identified as matrix, 296 and 107 analyses respectively. Thus a total of 1012 individual matrix measurements is used for the analysis (see Section 2.2). In the bulk composition all 1651 measurements (all analyses from areas M1 – M3, X1 and X2) are included. It can be seen that relative to bulk the matrix is enriched in the volatile elements Na and K, while the less volatile Li is depleted in the matrix. Furthermore, the matrix is depleted in moderately volatile elements, like Cr, P and S and in refractory elements, like Ca, Sc, Ti and V, compared to the Allende bulk composition. The second column of Table 1 reports the Allende matrix composition normalized to CI (Lodders et al., 2010). Compared to CI the.

Allende matrix is strongly depleted in volatile elements, which agrees with other studies of Allende (McSween, 1979; Bland et al., 2005; Scott and Krot, 2005; Gordon et al., 2007; Hezel and Palme, 2010). In addition

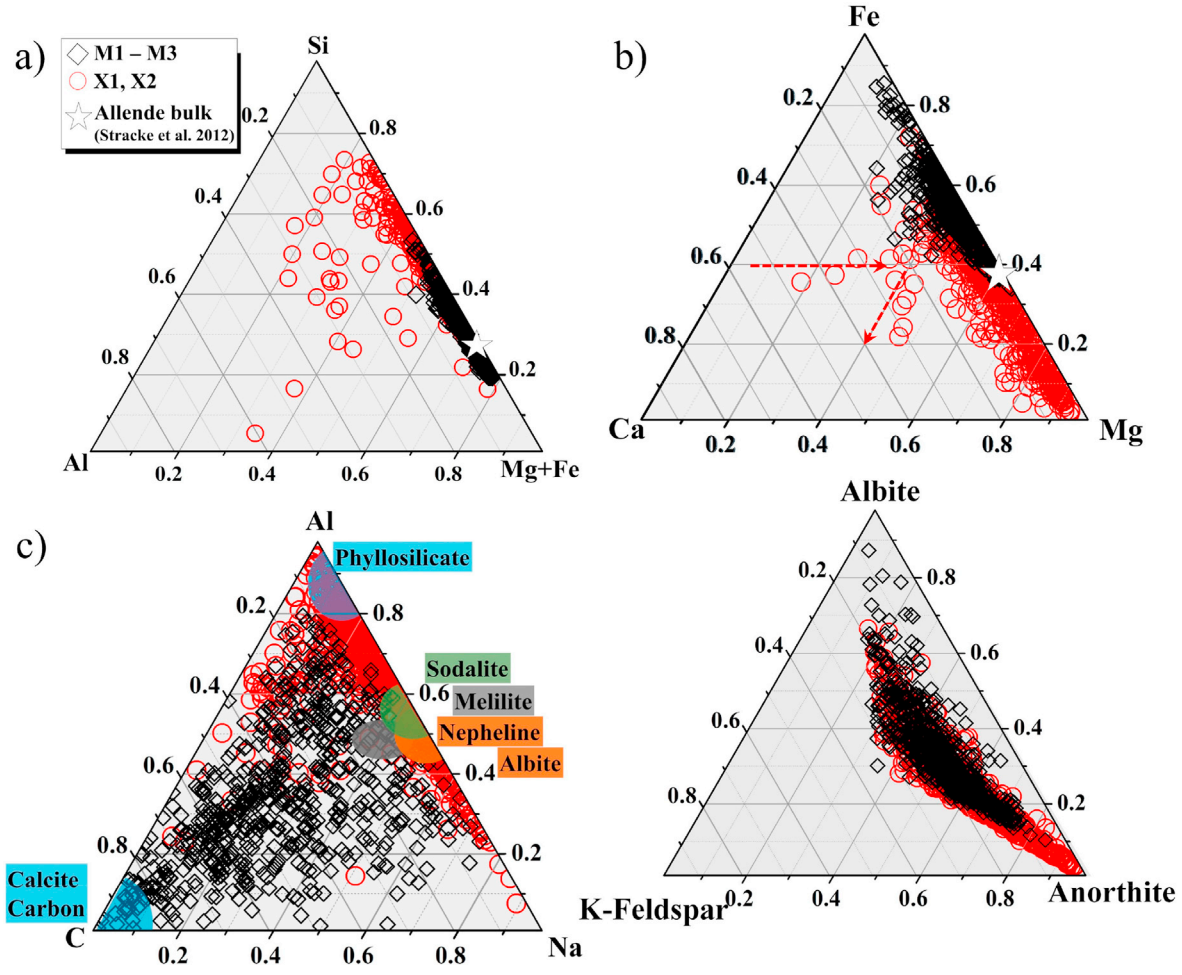

Fig. 6. Allende matrix mineralogy.
Ternary plots showing fractions of key elements or normative end-member minerals, in units of atomic fractions. The 609 measurements on Allende matrix (M1 – M3) show a much more homogeneous composition and a more Mg–Fe-rich component than the measurements in X1 and X2 (a), *(compare Fig. 1, 2 and 3). The matrix does not contain any minerals with high Al or Ca* (a, b). *The matrix is rich in C* (c) *and has a higher normative albite component compared to analyses of areas X1 and X2 that show a higher normative anorthite component* (d).

Table 1
Allende matrix.
Ratio of Allende matrix/bulk and ratio of Allende matrix/CI. Elements are ordered by their 50% condensation temperature.

	Matrix (LMS) relative to bulk (LMS) CI (Lodders et al., 2010)		T_{50} [K] (Lodders, 2003)	
C	1.019 ± 0.122	0.419 ± 0.028	40	volatile
O	0.921 ± 0.034	0.763 ± 0.012	180	
S	0.827 ± 0.035	0.130 ± 0.016	664	
Na	1.205 ± 0.251	0.763 ± 0.025	958	
K	1.229 ± 0.130	0.674 ± 0.038	1006	
Li	0.854 ± 0.033	0.375 ± 0.013	1142	
Mn	0.861 ± 0.064	0.830 ± 0.021	1158	mod.
P	0.480 ± 0.044	1.335 ± 0.022	1229	volatile
Cr	0.758 ± 0.039	2.643 ± 0.159	1296	
Si	0.829 ± 0.016	1.045 ± 0.008	1310	intermediate
Fe	1.066 ± 0.027	1.574 ± 0.032	1334	
Mg	0.812 ± 0.018	1.599 ± 0.033	1336	
Ni	0.830 ± 0.063	0.435 ± 0.111	1352	
Co	0.928 ± 0.183	2.974 ± 0.067	1353	
V	0.800 ± 0.082	3.197 ± 0.031	1429	refractory
Ca	0.888 ± 0.040	2.087 ± 0.057	1517	
Ti	0.813 ± 0.022	1.283 ± 0.005	1582	
Al	0.965 ± 0.076	0.911 ± 0.026	1653	
Sc	0.861 ± 0.088	3.360 ± 0.042	1659	

to the depletion in volatile elements, the Allende matrix is depleted in the moderately volatile transition metals Mn and Ni, while all other elements included in Table 1 show enrichment. High abundances compared to CI are observed for the refractory elements Co, V, Ca and Sc. When comparing the meteorite matrix with chondrules instead of Allende bulk, the depletion of Na and K relative to CI is even more distinct in the chondrules than in the matrix and the chondrules show an even more pronounced enrichment in refractory elements relative to CI. Table 2 shows the quantitative element abundances for all 19 elements analyzed in Allende matrix as measured with the LMS. In addition to the results from our measurements (first column "LMS") reference values from other studies are listed. All values are given in atomic number fraction, since the LMS measures numbers of atoms. Figures from the references were converted to atomic number fractions, if given in different units. For the conversion from weight % to atomic % the atomic weights from Meija et al. (2016) were used. The elements in Table 2 are sorted according to their condensation temperatures (T_{50}, Lodders, 2003). For easier comparison of the data sets given in Table 2, these data are shown as bar graphs in Figure A3 in Appendix A.

Abundance values for Li are included in our results, but not given in any other studies reporting element abundances for the Allende matrix. Abundances of C are given only in Clarke et al. (1971) and abundances of V and Sc are only provided by Rubin and Wasson (1987). Table 2 shows the differences of the element abundances for the various elements in different studies. Reported element abundances can be very different in different studies. For example, the abundance of Ca given in Rubin and Wasson (1987) is 16 times higher than the value provided in Zolensky et al. (1993) and 18 times higher than the Ca abundance given in Krot et al. (1997).

4.2. Matrix homogeneity

Fig. 5 shows how the data resulting from the moving average filter were processed (for V in this case). The measurements that create the flanks of the distributions are those with the highest deviation from the average from all 1012 matrix analyses. Fig. 2 shows that some of the matrix measurements are located very close to chondrules. However, there is no correlation of the highest deviations to the corresponding position of the moving average, the distance to the next chondrule in particular. Similarly, in all the ternary diagrams shown in Fig. 6, there is no correlation of the element abundance ratios with the individual matrix areas. When plotting the measurements of M1, M2 and M3 (black circles in Fig. 6) individually, the larger scatter (Fig. 6c) as well as the smaller scatter (Fig. 6a, b and d) remain, indicating that the matrix areas M1, M2 and M3 have similar chemical homogeneity.

The scale of the abundances of the elements included in our analyses ranges from the low ppm, e.g., for Sc, to percent, e.g., for O. Therefore, for comparing the results from different grid sizes of the moving average of the different elements X, the relative deviations instead of the absolute values were used to quantify the results. The absolute σ_X (x-axis in Fig. 5) were divided by the abundances derived from all 1012 matrix analyses (values in Table 2, "LMS"), called X_{all} in the following.

The relative deviations σ_X/X_{all} as a function of different grid sizes are displayed in Fig. 7a. The elements are sorted according to their T_{50} (Lodders, 2003). Representing the data as shown in Fig. 7a, an element with a perfectly heterogeneous distribution in the material would have a constant σ_X/X_{all} irrespective of the grid size, thus would appear as a horizontal line, where the level σ_X/X_{all} = const. describes the chemical inhomogeneity in the sample. In contrast, the decreasing trend of the data in Fig. 7a can be attributed to the improvement of the statistical accuracy resulting from more measurements, i.e., with larger grid size. Following the $\sqrt{n}$ – rule, the statistical uncertainty becomes smaller the more measurements n are included in the moving average grid. σ_X/X_{all} would be almost 0 for one single grid over all 609 matrix analyses (areas M1 – M3), and σ_X/X_{all} would be exactly 0 for one grid spanning over all 1012 matrix analyses, *including the matrix measurements in areas X1 and X2, since the matrix measurements in X1 and X2 were included for deriving X_{all}. Based on these two scenarios,* we devised a simple equation describing the spread in the measurements in Fig. 7a as.where σ_{inhom} describes the constant contribution by inhomogeneity of the sample, σ_{meas} the standard error introduced by the statistical measurement uncertainty and n the number of analyses. Both fit parameters, σ_{inhom} and σ_{meas}, have the unit σ_X/X_{all}. A typical example of fitting Equation 1 to the data can be found in appendix C, where the fit applied to the data of Al is shown in Figure C2.

$$\sigma = \sigma_{inhom} + \frac{\sigma_{meas}}{\sqrt{n}} \quad (1)$$

The parameters resulting from fitting Equation 1 to the data shown in Fig. 7a are displayed in Fig. 7b, with σ_{inhom} shown on the y-axis. The scale of the y-axis is reversed, so that chemical homogeneity is increasing from bottom to top. σ_{meas} is shown on the x-axis.

Fig. 7b shows that the elements that have the highest degree of homogeneity in the Allende matrix material are the rock-forming elements O, Si, Mg and Fe. These elements exhibit a variability of less than 5% ($\sigma_{inhom} < 0.05$) of their nominal abundance (Table 2, column "LMS"). Nearly on the same level of homogeneity are the elements Mn, Co, Ti, V, Al and Ni, although the measurement uncertainties σ_{meas} for Al and Ni are considerably larger than for the other elements. The elements that are the largest heterogeneity in Allende matrix material are C (20% variability), Ca and K (15%), and Li, S, and Na (10%).

5. Discussion

The element abundances in the Allende matrix measured with the LMS instrument are reported in Table 2 and compared with literature data. Since all studies on Allende matrix were carried out using different aliquots of Allende, small differences in the results are expected. Additionally, conventional techniques, e.g., wet chemical analyses, that require larger sample sizes bear the risk that these may not have been pure matrix material. The comprehensive data set presented in this study is based on chemical compositions determined from more than 1000 individual measurement positions. Thus, the resulting averages are representative for the composition of the Allende matrix.

The element abundances determined with the LMS (see Table 2), i.e., for S, K, Mg, Ca, Ti and Al, are within the ranges of values reported in the literature. For some of the elements the LMS measurements yielded

Table 2
Allende matrix composition.
In addition to the results from this study (column "LMS"), data from published studies are listed. All values are listed in atomic number fraction. In case volume or weight fraction was given in the reference, the values were converted accordingly (using atom masses from Meija et al. (2016). All values are given in plain fractions, except the numbers marked by an asterisk (*), which are given in [ppm]. A graphical representation of this table is given in Figure A3 in the Appendix. n.d. = not detected.

	LMS Present work	Clarke et al. (1971)	Rubin and Wasson (1987) "mxa"	"mxb"	McSween and Richardson (1977)	Zolensky et al. (1993)	Inoue et al. (2004)	Krot et al. (1997)
C	0.0082 ± 0.0011	0.018	*n.d.*		*n..d.*	*n..d.*	*n..d.*	*n..d.*
O	0.4704 ± 0.0175	0.519	*n.d.*		0.5197	0.5172	0.5237 ± 0.0188	0.5641 ± 0.0018
S	0.0150 ± 0.0006	0.022	*n.d.*		0.0086	0.0035	0.0064 ± 0.0003	*n..d.*
Na	0.0036 ± 0.0007	*n.d.*	0.0038	0.0026	0.0017	0.0004	0.0015 ± 0.0009	*n..d.*
***K**	202 ± 11	*n.d.*	191	290	52	*n.d.*	<263	*n..d.*
***Li**	1.8 ± 0.1	*n.d.*	*n.d.*		*n.d.*	*n.d.*	n.d.	*n..d.*
***Mn**	627 ± 47	909	958	1′285	721	697	735 ± 29	852 ± 136
***P**	896 ± 82	*n.d.*	*n.d.*		*n.d.*	522	551 ± 315	*n..d.*
***Cr**	2′895 ± 150	848	2′558	1′873	1′218	1′594	1′249 ± 338	445 ± 254
Si	0.0856 ± 0.0017	0.108	*n.d.*		0.1135	0.1216	0.1155 ± 0.0033	0.1396 ± 0.0028
Fe	0.1742 ± 0.0032	0.143	0.1572	0.1678	0.1081	0.1268	0.1246 ± 0.0037	0.1254 ± 0.0037
Mg	0.1355 ± 0.0030	0.156	0.2511	0.2345	0.1221	0.1266	0.1165 ± 0.0037	0.1553 ± 0.0066
Ni	0.0108 ± 0.0008	0.012	0.0037	0.0083	0.0060	0.0021	0.0053 ± 0.0001	*n..d.*
***Co**	549 ± 108	489	454	371	*n.d.*	*n.d.*	*n..d.*	*n..d.*
***V**	73 ± 7	*n.d.*	75	57	*n.d.*	*n.d.*	*n..d.*	*n..d.*
Ca	0.0103 ± 0.0005	0.014	0.0155	0.0165	0.0103	0.0010	0.0078 ± 0.0041	0.0009 ± 0.0009
***Ti**	260 ± 7	318	*n.d.*		274	278	<217	151 ± 121
***Al**	6′172 ± 483	7′060	19′094	17′067	10′989	8′194	9′431 ± 1′832	995 ± 853
***Sc**	9 ± 1	*n.d.*	7	5	*n.d.*	*n.d.*	*n..d.*	*n..d.*

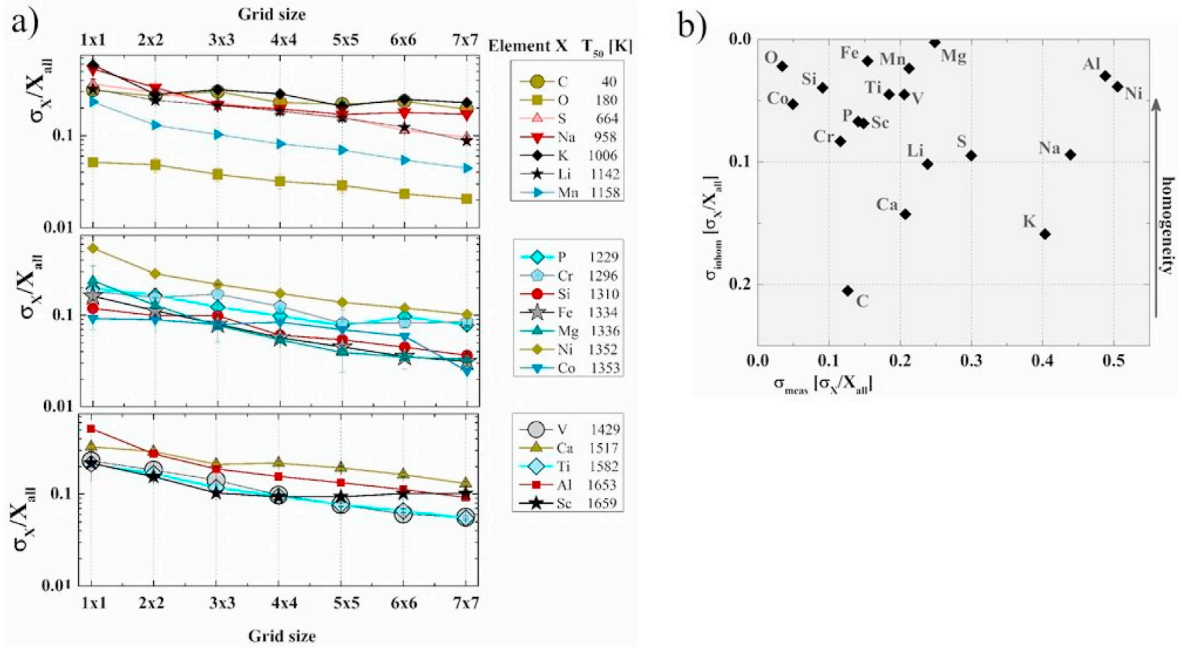

Fig. 7. Matrix homogeneity.
a) Standard deviation σ for different grid sizes of the moving average filter applied to the matrix areas M1 – M3. For comparison of different elements, σ was set in relation to the element abundance derived from all matrix analyses X_{all} (Table 2, "LMS"). T_{50}, displayed together with the elements in the legends, are taken from Lodders (2003). b) The fit parameters resulting from applying Equation 1 to the data shown in (a). The fit parameter σ_{inhom} is shown on the y-axis, which is reversed so that homogeneity of the elements is increasing from bottom to top.

abundances that are, without exception, lower (e.g., Mn) or higher (e.g., Fe, Cr) than the literature values. However, LMS measurements yield Fe (Matrix)/Fe (bulk) ≈ 1. We obtained higher Fe and lower Mg abundances compared to some studies (Clarke et al., 1971; Rubin and Wasson, 1987; Krot et al., 1997), but higher Fe abundance and also a slightly higher abundance of Mg compared to other studies (McSween and Richardson, 1977; Zolensky et al., 1993; Inoue et al., 2004). The Mg/Fe ratio (0.78 ± 0.02 for the LMS measurements) is similar to other studies, e.g., (Wark, 1979). A comparison of the element abundances measured with the LMS with the literature data reveals that the best agreement of the new results is with the data reported by Clarke et al. (1971), McSween and Richardson (1977), and Rubin and Wasson (1987) and the poorest agreement is observed with the data reported in Zolensky et al. (1993) and Krot et al. (1997).

Fig. 7 shows the degree of homogeneity/heterogeneity of the different elements in the pure matrix of Allende. The deviations of the individual analyses (i.e., 1 × 1 grid) are several tens of % for all elements except for O. With increasing grid size all σ decrease and approach a constant level. There is a systematic difference between σ and T_{50}. The statistical analysis reveals that the main mineral-forming elements O, Si,

Mg and Fe are, with a variability of less than 5%, the most homogeneously distributed elements in the matrix. The minor to trace elements Mn, Co, Ti, V and Ni show a similar degree of homogeneity. Although the alkali metals, as well as C, Ca and S, show larger heterogeneity, none of the elements that were measured show variability as a function of distance to a chondrule, which indicates a high degree of chemical and mineralogical homogeneity of the matrix material, even for intermediate and refractory elements.

The collective data points indicate that the matrix has an olivine rich composition and shows a shift towards higher Fe content, thus, higher Fe/Mg in the matrix minerals compared to chondrules (Fig. 6a). The areas X1 and X2 (matrix, chondrules) have a large portion of olivine as well, and the chondrules are enriched in elements that are typically contained in felsic minerals (e.g., Na, K, Ca, Al), particularly in feldspars. The Mg–Fe-rich minerals in Allende represent the major component that makes up carbonaceous chondrites in general. The high-Al regions in the matrix reveal the presence of CAI rich inclusions that are common in CV meteorites. The Ca-rich regions make up a small part of the matrix. The major portion of the matrix, and the chondrules have low Ca/(Fe + Mg) (see Fig. 6b).

Fig. 6d shows that the (normative) matrix plagioclase has a higher albite component, while in areas X1 and X2 many positions show essentially pure anorthite component, attesting to the higher volatile element content in the matrix compared to the chondrules. We find that, in contrast to Na and K, Li is depleted in the Allende matrix. A possible explanation for this could be that of all three alkali metals, Li has the highest condensation temperature (Table 1, last column), which could mean that all Li had already condensed into the chondrules by the time the matrix condensed.

When comparing the composition of matrix to the composition of chondrules, the major difference is the higher abundance of the refractory elements Co, V, Ca, Ti and Sc in chondrules. This difference reflects the high-temperature origin of the chondrules and the low-temperature formation of the matrix. This implies different formation conditions and possible different formation environments of these components. The occurrence of chondrules, chondrule fragments, CAIs and matrix in close association, each with their own thermal evolution and chemical composition can reflect the mixture of different components originating from places with different thermal evolution, possibly with different radial distances in the solar nebula (e.g. Takayama and Tomeoka, 2012), or matrix and chondrules formed in the same reservoir but at different times and under different thermal conditions.

The complementarity in the abundance of the refractory elements (Hezel and Palme, 2008) and the isotopes of refractory elements (e.g. Budde et al., 2016) between matrix and chondrules seems only possible if the chondrite parent body formed from a finite reservoir that was chemically closed at least during the interval when then refractory elements condensed and accreted. The correlation of depletion in moderately volatile elements and condensation temperature indicated that a gas phase was lost or did not condense during their condensation leading to the general depletion observed in all carbonaceous chondrites (e.g., Cassen, 2001). The subsequent condensation of highly volatile elements in chondritic abundances independent of the condensation temperature indicates complete condensation of the remaining elements without fractionation. The latter is possible if this final condensation was a sudden event, possibly the final collapse of remaining dust/gas cloud, where the matrix of Allende was enriched in volatiles elements relative to chondrules. The observation that the elements in the matrix are homogenously distributed indicates that no mineral fractionation happened during the accretion of matrix material. Gradual accretion of dust to pre-existing chondrules would result in the growth of the chondrule by addition of large dust rims that later make up the matrix. This accretion would result in fractionation of the minerals in the dust cloud. The accretion process must have maintained chemical complementary of matrix and chondrules in chondrites (Hezel and Palme, 2008), excluding contributions from different reservoirs of the solar nebula. The high degree of chemical homogeneity, independent of scale and location, implies that the matrix material did not consecutively accrete onto the earlier formed chondrules, as this would have resulted in mineral fractionation caused by the different sticking properties of the different minerals (e.g. Poppe et al., 2000). The difference in element abundances between chondrule and matrix indicates that there was element and thus mineral fractionation occurring during the formation of the chondrule precursor material, but this fractionation did not continue during dust accretion that formed the matrix of chondrites. Matrix material that accumulated layer by layer on earlier formed chondrules would show zones of different mineralogical and thus chemical composition. Such zones would presumably extend to several mm into the matrix material. The process of such a formation of zones is shown schematically in Fig. 8. The three measurement areas chosen on exclusively matrix material reach close to bordering chondrules (Fig. 2) and none shows discernible chemical zoning.

In contrast, a high degree of homogeneity of the matrix is revealed, which indicates that the matrix material formed independently from or in parallel with the chondrules and that the process that provoked all components forming the meteorite was a fast collapse of a chondrule-dust cloud that did not allow for the creation of zones. Thus, the collapse must have occurred on a timescale that did not allow for a fractionation of different mineral phases in the condensing and cooling solar nebula. This rapid process led to the accretion of chondrules together with dust into the parent body by a rapid process possibly akin to pebble accretion (Lambrechts and Johansen, 2012).

6. Conclusion

Laser ablation/ionization mass spectrometry (LIMS) is a well-suited analytical technique for obtaining spatially resolved quantitative element abundances of rocky material in situ. Analyses of different components, particularly matrix and chondrules, in the primitive carbonaceous chondrite Allende provide a two-dimensional image of the distribution of selected elements in this early solar system material. Also owing to earlier studies of the calibration procedures (Neuland et al., 2016), the abundances of 19 elements (C, O, S, Na, K, Li, Mn, P, Cr, Si, Fe, Mg, Ni, Co, V, Ca, Ti, Al, Sc) in the Allende matrix were determined quantitatively. Although the LMS might have a lower spatial resolution, lower sensitivity and mass resolution than the much larger LIMS-type laboratory instruments, this study shows that its performance is more than sufficient for collecting highly valuable element abundance data to study the chemical composition, mineralogy and homogeneity of rocky materials, for example in situ analysis on a planetary body, a meteorite parent for example.

The chemical data obtained for the Allende matrix composition in this study is in general agreement with published values. However, using the LMS instrument it is possible to collect a much larger data set in a remarkably short measurement time compared to more conventional laboratory techniques. Five selected areas on the sample were investigated with high spatial resolution using our miniature LMS. The 1651 positions that were analyzed, each of about 12 μm in diameter, reveal the element distribution in the meteorite sample from major to trace elements, and provide constraints on the length scale of chemical heterogeneity in the material. Out of the 1651 spot analyses 1012 are located on the Allende matrix. The element abundances obtained from the analyses can be related the mineralogical composition of the fine grained meteorite matrix. In agreement with earlier studies of Allende, the matrix mostly consists of Fe-rich olivine and it is enriched in the more volatile elements (e.g., K and Na) and depleted in the refractory elements (e.g., Ca, Sc) relative to the bulk material.

The measurements in three selected areas on exclusively Allende matrix material allow a detailed analysis of the degree of homogeneity of this meteorite component. A moving average filter was applied to derive the standard deviation of the chemical composition of matrix material on different scales. While the smallest analyzed scale is the distance of 50 μm

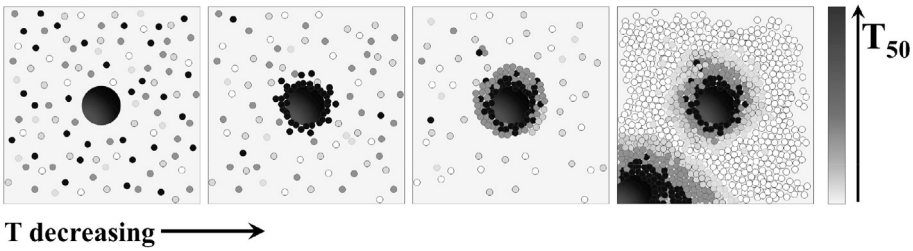

Fig. 8. Zones around chondrules.
A formation of the meteorite matrix by a layer-by-layer accretion of the residual gas onto the chondrules/chondrule rims would have led to zones that would reach out several mm or even cm into the matrix material.

between single measurement positions, grid sizes up to 7 × 7 positions, which equals an area of 0.09 mm^2, were included. A fit function describes the deviation of the chemical composition as a function of the number of analyses included. This fit function contains two parameters that describe the deviation attributed to an inhomogeneous distribution of an element in the matrix material and the deviation introduced by statistical measurement uncertainties. From the homogeneity analyses it can be concluded that the process that merged chondrules and matrix did not cause element or mineral fractionation and thus, must have been a fast collapse rather than a slow layer-wise accumulation of matrix material on the chondrules.

Author statement

I herewith confirm that all authors have agreed with the revised version of the manuscript.

In the original work the co-authors have contributed as follows:

Dr. Maike Brigitte Neuland (corresponding author): Experiment Design and Management, Laboratory measurements, Method development, Data analysis.

Prof. Peter Wurz: Management, discussion and conclusion.

Prof. Klaus Mezger: Mineralogical analysis, discussion and conclusion.

Dr. Andreas Riedo: LMS instrument operation and optimization, laboratory experiments, discussion.

Dr. Marek Tulej: LMS instrument operation and optimization, discussion.

All authors have contributed to revising the manuscript.

Declaration of competing interest

The authors declare that they have no known competing financial interests or personal relationships that could have appeared to influence the work reported in this paper.

Acknowledgments

This study is funded by the Swiss National Science Foundation (SNF). The data are available via the Open Science Forum (OSF), under https://osf.io/aj3xc/.

Appendix

A. *Data Selection and Element Analysis*

In this study all mass spectra, similar to the example mass spectrum shown in Figure A1, contain the accumulated data from 36 000 single laser shots. The areas of all peaks in the mass spectra are derived independently from the high gain (HG), medium gain (MG) and low gain (LG) data. After identification of the saturated isotope peaks in the HG, the data from the different channels are combined according to the gain, for element analysis. Element abundances are only derived from the non-isobaric isotopes. We calculated, e.g., that the mass peak at 40 amu consists of >99.9% ^{40}Ca and thus is the most suitable forcalculating the abundance of Ca. Due to interference with Ti the abundance of V was calculated from ^{51}V only. Similar considerations were taken for all other elements included in the analyses. Table A1 lists isotopes that, if detected (LG, Fig. A1 right) and not saturated (HG, Fig. A1 left), were used for deriving the elements. The resulting peak area corresponds to the number of atoms of the corresponding element contained in the volume of the ablation crater. Therefore, after calibration of the element sensitivity, the ratio of one element to the set of all elements corresponds to the atomic number fraction.

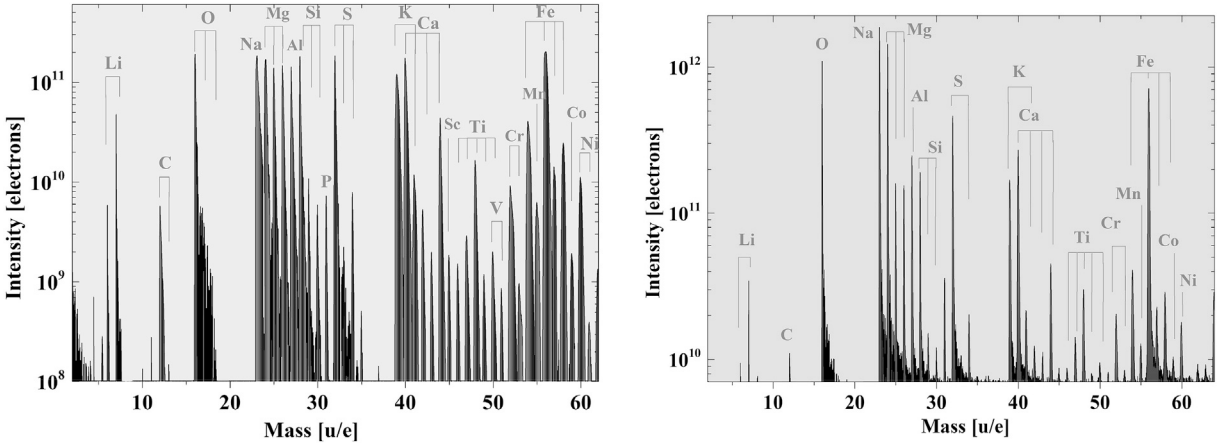

Fig. A1. Mass Spectra.
Mass spectrum of Allende (area M1) with several elements assigned to the mass peaks. Highly abundant elements are saturated in the high gain (HG) channel (left). For the analyses of major elements the data from the low gain (LG) channel (right) is used, while minor elements are detected with high sensitivity in the HG channel.

Table A1
Isotopes included in the element analyses.
Several of the elements included in this study are affected by isobaric interferences with other elements. Isotopes shown in parentheses were used only if visible (in the LG) and not saturated (in the HG).

Element	Derived from isotopes [mass number]	
	HG	LG
C	12, 13	12, (13)
O	(16), 17, 18	16, (17, 18)
S	32, 34	32, (34)
Na	(23)	23
K	(39), 41	39, 41
Li	6, (7)	(6), 7
Mn	55	(55)
P	31	(31)
Cr	52, 53	52, (53)
Si	(28), 29, 30	28, (29), (30)
Fe	54, (56), 57	54, 56, (57)
Mg	25, 26	24, 25, 26
Ni	60, 61	(60, 61)
Co	59	(59)
V	51	(51)
Ca	40, 42, (43), 44	40, 44
Ti	47, 48, 49	(47), 48, (49)
Al	27	27
Sc	45	(45)

Section 2.2 describes the analytical methods used to determine the chemical composition of individual measurement points on a sample of Allende meteorite and how these were classified as either Allende matrix or other material with the help of optical images and the element maps resulting from the LMS measurements. The left upper panel of Figure A2 shows the measurement area X2. This image is identical to Fig. 3b in the main text, but cropped to the area where measurements were conducted. Furthermore, the borders of material that is optically distinguishable is marked by lines (upper left panel). The other three panels of Figure A2 show, as an example, the element maps for Si, Al and Fe derived from the LMS measurements in this area.

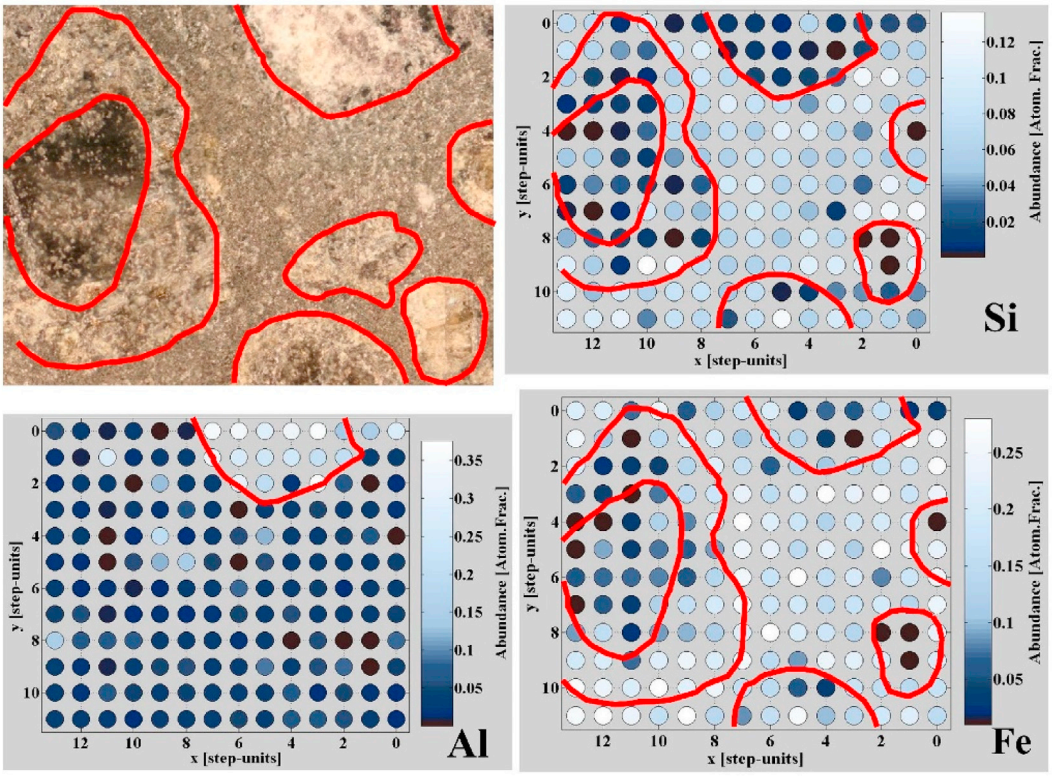

Fig. A2. Element maps.
Element maps combined with optical images were used to select measurements representing Allende matrix from measurements on other material. Darker co lors correspond to lower abundances. The example shows maps of Si, Al and Fe of area X

2 (compare Figs. 1 and 3b in main text).

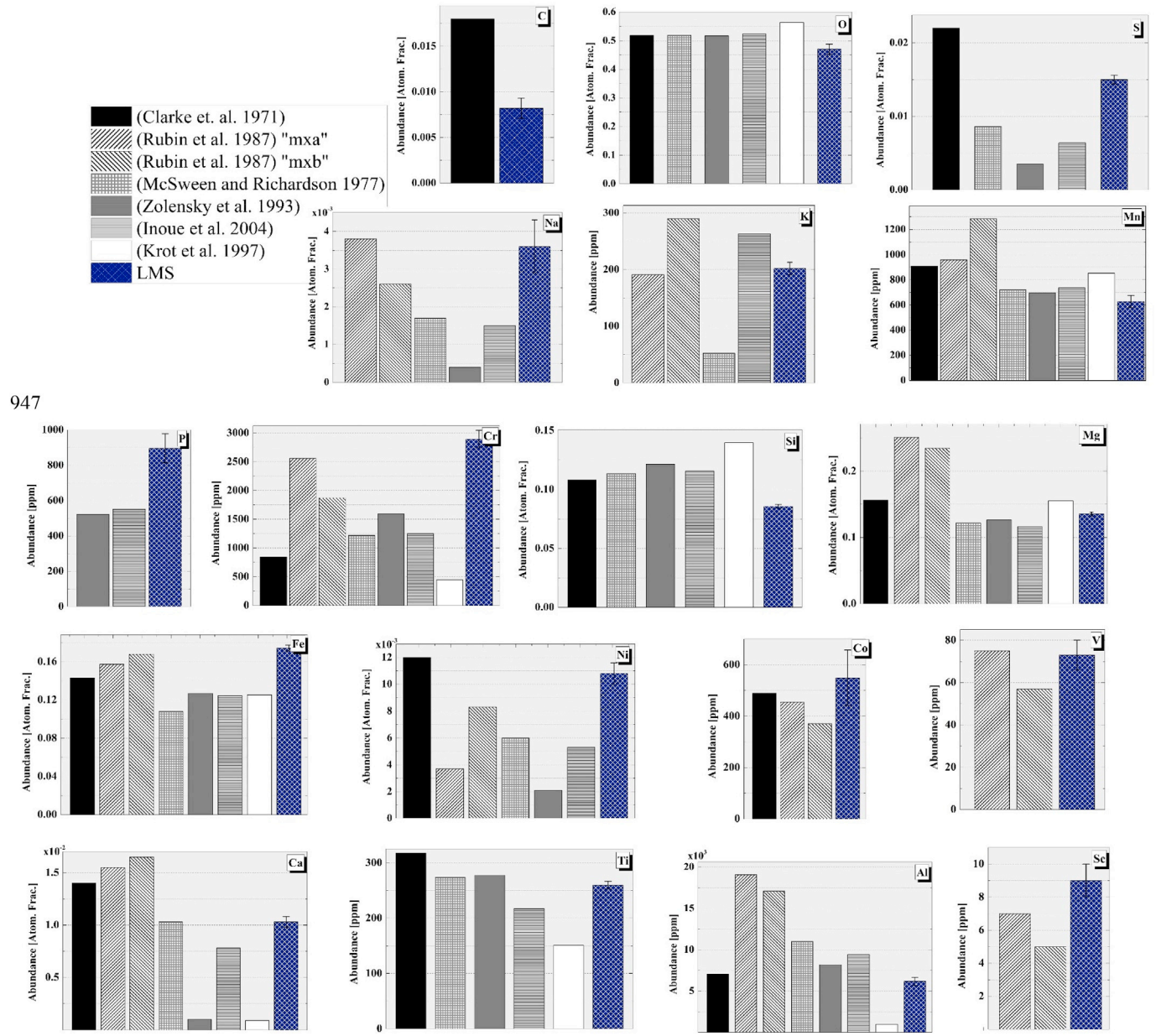

947

Fig. A3. The abundances of 18 elements in Allende matrix.
The chemical composition of the Allende matrix (Table 2 in main text) is visualized in bar graphs. The abundances measured in this study with the LMS are compared to literature values. The legend is the same for all 18 graphs. The results for Li are not included in the graph, because no literature value exists for comparison.

B. Calibration

As described in Section 3.2, the relative sensitivity coefficients (RSCs) were derived by using the complete data set of measurements (M1 – M3, X1 and X2) representing Allende bulk. The data reported in Stracke et al. (2012) are used as a reference for calibration. For elements that are not included in Stracke et al. (2012), Allende bulk data from Mason (1975), Jarosewich (1990) and Clarke et al. (1971) were consulted. In Table B1 the reference values that were used for the final calculation of the RSCs are listed in the last column.

In Figure B1a the resulting RSCs are shown as the correlation of the LMS measured and the reference element abundances. In this representation the distance of a data point to the diagonal line (shown as a solid line), measured perpendicularly, equals the RSC. We chose a representation of the data similar to the plots shown in Neuland et al. (2016), where the symbols account for different measurement campaigns and the colors refer to the different elements. In addition to the measurements with the fs-laser ion source (this study, diamond symbols) the RSC data from composition measurements of Allende with a ns-laser ion.

Table B1
Allende bulk literature values.
The relative sensitivity coefficients (RSCs) were calculated by using the values from Stracke et al. (2012) as a reference for Allende bulk. For the elements not evaluated in the latter, average values from Mason (1975), Jarosewich (1990) and Clarke et al. (1971) were used. Numbers that are displayed in bold font are key values to determine the value finally used (last column). All values are given in plain number fractions. Elements marked by an asterisk (*) are given in [ppm]. n.d. = not determined

	Stracke et al. (2012)	Mason (1975)	Jarosewich (1990)	Clarke et al. (1971) set 1	set2	Used for calibration
C	*n.d.*	**0.003**	**0.006**	**0.014**		0.009
O	**0.511**	0.370	*n.d.*	0.528		0.511
S	*n.d.*	**0.021**	**0.015**	**0.018**		0.019
Na	*n.d.*	**0.003**	*n.d.*	0.003		0.003
K*	*n.d.*	**250**	*n.d.*	**121**		185
Li*	*n.d.*	**2**	*n.d.*	*n.d.*		2
Mn*	**728**	1500	610	725	723	728
P*	**1′868**	1100	*n.d.*	264		1868
Cr*	**3′821**	3600	1′600	767	795	3821
Si	**0.103**	0.160	0.140	0.108		0.103
Fe	**0.115**	0.236	0.103	0.123		0.115
Mg	**0.167**	0.149	0.150	0.175		0.167
Ni	**0.013**	0.014	0.006	0.008	0.009	0.013
Co*	**591**	610	250	348	347	591
V*	**92**	90	*n.d.*	*n.d.*		92
Ca	**0.012**	0.019	*n.d.*	0.013		0.012
Ti*	**320**	900	450	381	333	320
Al*	**6′394**	17 400	15 000	7530	7113	6394
Sc*	*n.d.*	**11**	*n.d.*	*n.d.*		11

source (Neuland et al., 2014) (circles) were added to the graph. The measurements with the fs-laser system allowed the evaluation of more elements than the ns-laser measurements. In particular, the ns-laser data do not allow the quantitative evaluation of the alkali metals nor P and O. This is due to the plasma processes in the laser ablation plume of ns-laser pulses. The fs-laser offers a much higher power, much shorter pulse width and thus completely different ablation conditions (Ohata et al., 2014; Russo et al., 2002). Figure B1a shows that in general the RSCs for measurements with the fs-laser ion source are closer to 1 than for the measurements with the ns-laser, which is most distinct for Si, S, C and Ni. This agrees with the results presented in Riedo et al. (2013a), where composition measurements of the standard reference sample NIST SRM661 with the LMS with both laser systems are compared. For several elements the RSCs develop in a different direction. For example, the RSCs of Ti, Sc and Ca are closer to 1 for the measurements with the ns-laser. The particularly high RSCs of these elements are also observed in the measurements on geological standard reference materials (Neuland et al., 2016).

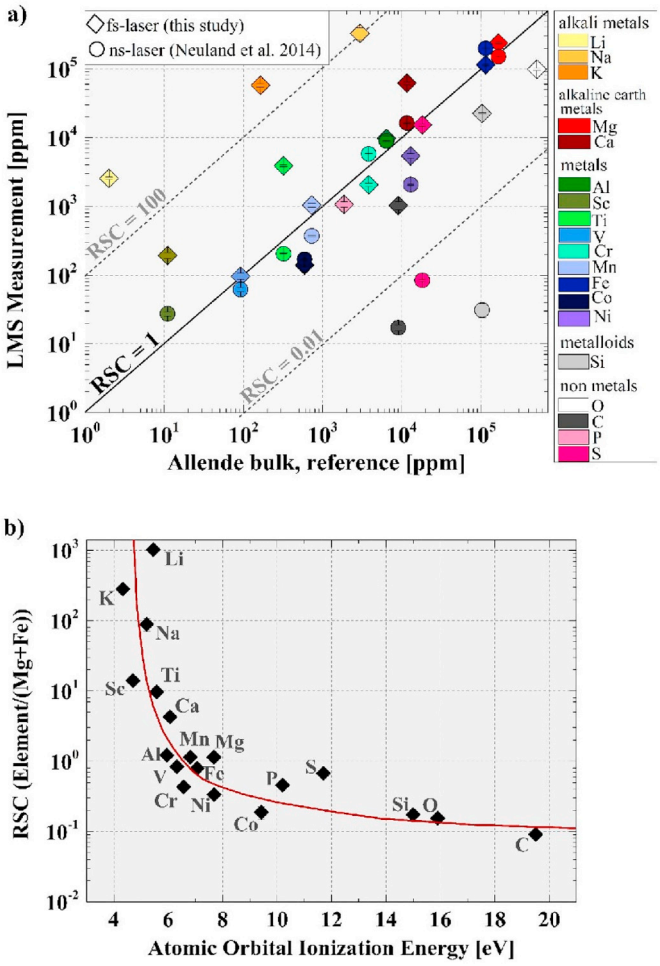

Fig. B1. Relative sensitivity coefficients.
a) Relative sensitivity coefficients as the correlation of LMS measured abundance (y-axis) and Allende bulk element abundance from a reference (see appendix, Table B1). Additionally, circular data points show the RSCs from Neuland et al. (2014), where a ns-laser ionization source was applied for measuring the chemical composition of the same Allende sample. b) The RSC values, each relative to (Mg + Fe) as a function of the atomic orbital ionization energies (Gray, 1964). According to Zhang et al. (2015) a fit was applied to the data, providing additional validation of the RSCs.

In Zhang et al. (2015), Fe was used as a reference element as this is the major component of the solid standard samples investigated by the authors. For the same reason, O was used as a reference element in the calibration studies presented in Neuland et al. (2016). While O is also the major component of the minerals in Allende, it is, at the same time, an element for which the values in the literature differ slightly, which is of disadvantage when using the element as a reference. Since Fe and Mg are major elements in Allende minerals, and the values for (Fe + Mg) are more consistent throughout different sources, we used (Fe + Mg) as a reference for applying the fit from Zhang et al. (2015). The resulting fit is consistent with former RSC studies, when using the second AOIEs instead of the first. A reason for this could be that ionization from an orbital with higher three-dimensional symmetry (thus s- or d-instead of p-orbital) has a much higher probability for ionization by the directional laser photons. However, this needs much more detailed investigation before firm conclusions can be drawn. With the AOIEs from Gray (1964) the fit, shown in Figure B1b, results in an electron plasma temperature of $T_e = 1.21 \cdot 10^5$ K and an electron density of $N_e = 9.05 \cdot 10^{23} cm^{-3}$, which is in good agreement with former RSC studies. Furthermore, when introducing the ionization potential of the reference element as a fit parameter as well, this results in an AOIE of (Mg + Fe) = 7.976 eV. Since the individual values for Mg and Fe are 7.68 eV and 7.07 eV (Gray, 1964), this is another strong support for the reliability of the applied procedure. Neuland et al. (2016) showed that a correlation exists between the elements respectively the element groups and the atomic orbital, from which the atoms are ionized. Additionally, in the same publication, we showed that the function developed by Zhang et al. (2015) is suitable to fit the correlation of the RSCs and the atomic orbital ionization energy (AOIE) for data measured with the LMS.

C. *Homogeneity Analysis*

As described in Section 3.3 the matrix homogeneity was analyzed by applying a moving average filter to the data of the matrix areas M1 – M3. In addition to Fig. 5, the histograms (deviations σ_X of moving grid average to element abundance derived from all 1012 matrix measurements) of Li, Si and Sc for all grid sizes are shown in Fig. C1.

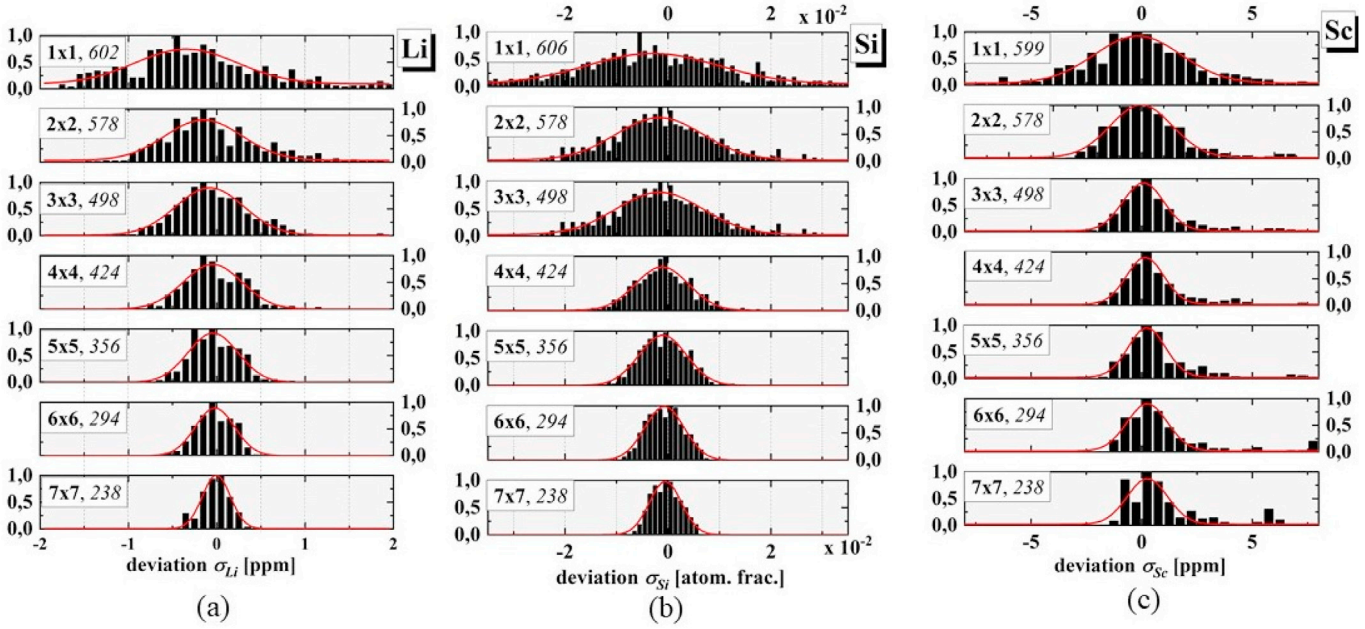

Fig. C1. Homogeneity analysis, examples.
Histograms for all different grid sizes of the moving average for Li, Si and Sc analyses in the matrix areas M1 – M3, additionally to Fig. 5, where the histograms for V are shown. The number in italics in each panel behind the grid size gives the number of entries of the according histogram. This number is decreasing with increasing grid size. .

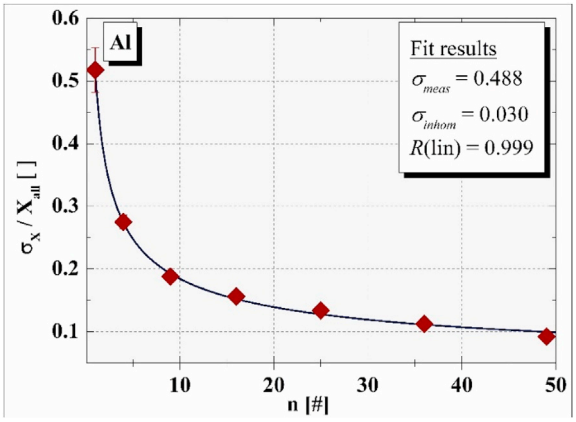

Fig. C2. Homogeneity analysis, fit.
A fit function (Eq. (1)) was introduced containing parameters for the statistical measurement error σ_{meas} and the abundance deviations due to inhomogeneity σ_{inhom} (both in units of the dimensionless fraction σ_x/X_{all}). According to the $\sqrt{n}$ – rule the width of the Gaussians is decreasing, when more measurements n are included. This example shows the fit applied to the data for Al (compare Fig. 7a).

References

Abreu, N.N., Brearley, A.J., 2010. Early solar system processes recorded in the matrices of two highly pristine CR3 carbonaceous chondrites. Geochem. Cosmochim. Acta 74, 1146–1171. https://doi.org/10.1016/j.gca.2009.11.009.

Alexander, Conel M.O'D., 2005. Re-examining the role of chondrules in producing the elemental fractionations in chondrites. Meteoritics Planet Sci. 40 (7), 943–965. https://doi.org/10.1111/j.1945-5100.2005.tb00166.x.

Alexander, Conel M. O'D., Ebel, D.S., 2012. Questions, questions: can the contradiction between the petrologic, isotopic, thermodynamic, and astrophysical constraints on the chondrules formation be resolved? Meteoritics Planet Sci. 47 (7), 1157–1175. https://doi.org/10.1111/j.1945-5100.2011.01308.x.

Amelin, Y., Krot, A.N., Hutcheon, I.D., Ulyanov, A.A., 2002. Lead isotopic ages of chondrules and calcium-aluminum-rich inclusions. Science 297, 1678–1683. https://doi.org/10.1126/science.1073950.

Becker, J.S., 2007. Inorganic Mass Spectrometry: Principles and Applications. John Wiley & Sons, ISBN 978-0-470-01200-0.

Bland, P.A., Alard, O., Benedix, G.K., Kearsly, A.T., Menzies, O.N., Watt, L.E., Rogers, N.W., 2005. Volatile fractionation in the early solar system and chondrules/matrix complementarity. Proc. Natl. Acad. Sci. U.S.A. 102, 13755–13760. https://doi.org/10.1073/pnas.0501885102.

Brearley, A.J., 1999. Origin of graphitic carbon and pentlandite in matrix olivines in the Allende meteorite. Science 285, 1380–1382. https://doi.org/10.1126/science.285.5432.1380.

Brinckerhoff, W.B., McEntire, R.W., Cheng, A.F., 2002. Reflectron Time-Of-Flight Mass Spectrometer (REMAS) Instrumentation. NASA progress report, p. 30. ID20020041925.

Budde, G., Burkhardt, C., Brennecka, G.A., Fischer-Gödde, M., Kruijer, T.S., Kleine, T., 2016. Molybdenum isotopic evidence for the origin of chondrules and a distinct genetic heritage of carbonaceous and non-carbonaceous meteorites. Earth Planet Sci. Lett. 454, 293–303. https://doi.org/10.1016/j.epsl.2016.09.020.

Buseck, P.R., Hua, X., 1993. Matrices of carbonaceous chondrite meteorites. Annu. Rev. Earth Planet Sci. 21, 255–305. https://doi.org/10.1146/annurev.ea.21.050193.001351.

Cassen, P., 2001. Nebular thermal evolution and the properties of primitive planetary material. Meteoritics Planet Sci. 36, 671–700. https://doi.org/10.1111/j.1945-5100.2001.tb01908.x.

Clarke, R.S., Jarosewich, E., Mason, B., Nelen, J., Gomez, M., Hyde, J.R., 1971. The Allende, Mexico, meteorite shower, smiths. C. Earth Sci. 5, 1–53. https://doi.org/10.5479/si.00810274.5.1.

Desch, S.J., Morris, M.A., Connolly Jr., H.C., Boss, A.P., 2012. The importance of experiments: constraints on chondrule formation. Meteoritics Planet Sci. 47, 1139. https://doi.org/10.1111/j.1945-5100.2012.01357.x.

Frank, D.R., Zolensky, M.E., Le, L., 2014. Olivine in terminal particles of Stardust aerogel tracks and analogous grains in chondrite matrix. Geochem. Cosmochim. Acta 142, 240–259. https://doi.org/10.1016/j.gca.2014.05.037.

Friend, P., Hezel, D.C., Mucerschi, D., 2016. The conditions of chondrules formation, Part II: Open system. Geochem. Cosmochim. Acta 173, 198–209. https://doi.org/10.1016/j.gca.2015.10.026.

Gordon, S.H., Hammond, S.J., Rogers, N.W., Charlier, B.L.A., Bland, P.A., 2007. Constraints on volatile depletion from chondrite matrix. LPSC XXXVIII, 2, 1819.

Gray, H., 1964. Electrons and Chemical Bonding. W.A. Benjamin Inc.

Hezel, D.C., Palme, H., 2008. Constraints for chondrule formation from Ca-Al distribution in carbonaceous chondrites, Earth Planet. Sci. Lett. 265 (3–4), 716–725. https://doi.org/10.1016/j.epsl.2007.11.003.

Hezel, D.C., Palme, H., 2010. The chemical relationship between chondrules and matrix and the chondrules matrix complementarity. Earth Planet Sci. Lett. 294, 85–93. https://doi.org/10.1016/j.epsl.2010.03.008.

Inoue, M., Kimuara, M., Nakamura, N., 2004. REE abundances in the matrix of the Allende (CV) meteorite: implications for matrix origin. Meteoritics Planet Sci. 39, 599–608. https://doi.org/10.1111/j.1945-5100.2004.tb00922.x.

Jacquet, E., Alard, O., Gounelle, M., 2015. Trace element geochemistry of ordinary chondrite chondrules: the type I/typeII chondrule dichotomy. Geochem. Cosmochim. Acta 155. https://doi.org/10.1016/j.gca.2015.02.005, 47-47.

Jarosewich, E., 1990. Chemical analyses of meteorites: a compilation of stony and iron meteorite analyses. Meteoritics 25, 323–337. https://doi.org/10.1111/j.1945-5100.1990.tb00717.x.

Jones, R.H., 2012. Petrographic constraints on the diversity of chondrules reservoirs in the protoplanetary disc. Meteoritics Planet Sci. 47 (7), 1176–1190. https://doi.org/10.1111/j.1945-5100.2011.01327.x.

Krot, A.N., Scott, E.R.D., Zolensky, M.E., 1997. Origin of fayalitic olivine rims and lath-shaped matrix olivine in the CV3 chondrite Allende and its dark inclusions. Meteoritics Planet Sci. 32, 31–49. https://doi.org/10.1111/j.1945-5100.1997.tb01238.x.

Lambrechts, M., Johansen, A., 2012. Rapid growth of gas-giant cores by pebble accretion. Astron. Astrophys. 544, A32. https://doi.org/10.1051/0004-6361/201219127.

Li, L., Zhang, B., Huang, R., Hang, W., He, J., Huang, B., 2010. Laser ionization orthogonal time-of-flight mass spectrometry for simultaneous determination of nonmetallic elements in solids. Anal. Chem. 82, 1949–1953. https://doi.org/10.1021/ac9026912.

Lodders, K., 2003. Solar system Abundances and condensation temperatures of the elements. Astrophys. J. 591, 1220–1246. https://doi.org/10.1086/375492.

Lodders, K., 2010. Solar system Abundances of the elements in: principles and perspectives in cosmochemistry. In: Goswami, A., Reddy, B.E. (Eds.), Astrophys. Space Sci. Proc. Springer Berlin Heidelberg. https://doi.org/10.1007/978-3-642-10352-0_8.

MacPherson G.J., Glenn, Boss A., Alan, 2011. /pnas.1110051108. Proc. Natl. Acad. Sci. USA 108 (48), 19152–19158. https://doi.org/10.1073/pnas.1110051108.

Mason, B., 1975. The Allende meteorite – cosmochemistry's rosetta stone. Accounts Chem. Res. 8 (7), 217–224. https://doi.org/10.1021/ar50091a001.

McSween, H.Y., Richardson, S.M., 1977. The composition of carbonaceous chondrite matrix. Geochem. Cosmochim. Acta 41, 1145–1161. https://doi.org/10.1016/0016-7037(77)90110-7.

McSween, H.Y., 1979. Are carbonaceous chondrites primitive or processed? Rev. Geophys. Space Phys. 17, 1059–1078. https://doi.org/10.1029/RG017i005p01059.

Meija, J., Coplen, T.B., Berglund, M., Brand, E.A., DeBièvre, P., Gröning, M., Holden, N.E., Irrgeher, J., Loss, R.D., Walczyk, T., Prohaska, T., 2016. Atomic weights of the elements 2013, (IUPAC technical report). Pure Appl. Chem. 88 (3), 265–291. https://doi.org/10.1515/pac-2015-0305.

Meyer, S., Riedo, A., Neuland, M.B., Tulej, M., Wurz, P., 2017. Fully automatic and precise data analysis developed for time- of-flight mass spectrometry. J. Mass Spectrom. 52, 580–590. https://doi.org/10.1002/jms.3964.

Morfill, G.E., Durisen, R.H., Turner, G.W., 1998. An accretion rim constraint on chondrule formation theories. Icarus 134 (1), 180–184. https://doi.org/10.1006/icar.1998.5948.

Morlok, A., Bischoff, A., Stephan, T., Floss, C., Zinner, E., Jessberger, E.K., 2006. Brecciation and chemical heterogeneities of CI chondrites. Geochem. Cosmochim. Acta 70, 5371–5394. https://doi.org/10.1016/j.gca.2006.08.007.

Neuland, M.B., Meyer, S., Mezger, K., Riedo, A., Tulej, M., Wurz, P., 2014. Probing the Allende meteorite with a miniature laser-ablation mass analyser for space application, Planet. Space Sci 101, 196–209. https://doi.org/10.1016/j.pss.2014.03.009.

Neuland, M.B., Grimaudo, V., Mezger, K., Moreno-Garcia, P., Riedo, A., Tulej, M., Wurz, P., 2016. Quantitative measurement of the chemical composition of geological standards with a miniature laser ablation/ionization mass spectrometer designed for in situ application in space research. Meas. Sci. Technol. 27, 035904 https://doi.org/10.1088/0957-0233/27/3/035904.

Norton, O.R., 2002. The Cambridge Encyclopedia of Meteorites. Cambridge University Press, ISBN 9780521621434.

Ohata, M., Tabersky, D., Glaus, R., Koch, J., Hattendorf, B., Günther, D., 2014. Comparison of 795nm and 265nm femtosecond and 193nm nanosecond laser ablation inductively coupled plasma mass spectrometry for the quantitative multi-element analysis of glass materials. Anal. At. Spectrom. 29 (8), 1309–1506. https://doi.org/10.1039/C4JA00030G.

Olsen, M.B., Wielandt, D., Schiller, M., Van Kooten, E.M., Bizzaro, M., 2016. Magnesium and 54Cr isotope composition of carbonaceous chondrules – insights into early disk processes. Geochem. Cosmochim. Acta 191, 118–138. https://doi.org/10.1016/j.gca.2016.07.011.

Palme, H., Hezel, D.C., Ebel, D.S., 2015. The origin of chondrules: constraints from matrix composition and matrix- chondrule complementary. Earth Planet Sci. Lett. 411, 11–19. https://doi.org/10.1016/j.epsl.2014.11.033.

Poppe, T., Blum, J., Henning, T., 2000. Analogous experiments on the stickiness of micron-sized preplanetary dust. Astrophys. J. 533, 454–471. https://doi.org/10.1086/308626/.

Riedo, A., Neuland, M., Meyer, S., Tulej, M., Wurz, P., 2013a. Coupling of LMS with a fs-laser ablation ion source: elemental and isotope composition measurements. Anal. Atom.Spectrom. 28, 256–1269. https://doi.org/10.1039/C3JA50117E.

Riedo, A., Bieler, A., Neuland, M.B., Tulej, M., Wurz, P., 2013b. Performance evaluation of a minature laser ablation time-of- flight mass spectrometer designed for in situ investigations in planetary space research. J. Mass Spectrom. 48, 1–15. https://doi.org/10.1002/jms.3104.

Riedo, A., Meyer, S., Heredia, B., Neuland, M.B., Bieler, A., Tulej, M., Leya, I., Iakovleva, M., Mezger, K., Wurz, P., 2013c. High accurate isotope measurements by a miniaturized laser ablation mass spectrometer designed for in situ investigations on planetary surfaces. Planet. Space Sci. 87, 1–13. https://doi.org/10.1016/j.pss.2013.09.007.

Riedo, A., Grimaudo, V., Moreno-Garcia, P., Neuland, M.B., Tulej, M., Broekmann, P., Wurz, P., 2016. Laser ablation/ionisation mass spectrometry: sensitive and quantitative chemical depth profiling of solid materials. Chimia 70, 268–273. https://doi.org/10.2533/chimia.2016.268.

Riedo, A., Tulej, M., Rohner, U., Wurz, P., 2017. High-speed strip-line multi-anode multichannel plate detector system. Rev. Sci. Instrum. 88 https://doi.org/10.1063/1.4981813, 045114.

Rohner, U., Whitby, J.A., Wurz, P., 2003. A miniature laser ablation time-of-flight mass spectrometer for in situ planetary exploration. Meas. Sci. Technol. 14, 2159–2164. https://doi.org/10.1088/0957-0233/14/12/017.

Rubin, A.E., Wasson, J.T., 1987. Chondrules, matrix and coarse-grained chondrule rims in Allende meteorite: origin, relationships and possible precursor components. Geochem. Cosmochim. Acta 51, 1923–1937. https://doi.org/10.1016/0016-7037(87)90182-7.

Russo, R.E., Mao, X., Mao, S.S., 2002. The Physics of laser ablation in microchemical analysis. Anal. Chem. 74 (3), 70–77. https://doi.org/10.1021/ac0219445.

Schrader, D.L., Fu, R.R., Desch, S.J., Davidson, J., 2018. The background temperature of the protoplanetary disk within the first four million years of the Solar System. Earth Planet Sci. Lett. 594, 30–37. https://doi.org/10.1016/j.epsl.2018.09.030.

Scott, E.R.D., Krot, A.N., Reipurth, B., 2005. Chondritic meteorites and the high-temperature nebular origins of their components. In: Chondrites and the Protoplanetary Disk, ASP Conference Series, vol. 341, pp. 15–53.

Simon, J.I., Cuzzi, J.N., McCain, K.A., Cato, M.J., Christoffersen, P.A., Fisher, K.R., Srinivasan, P., Tait, A.W., Olson, D.M., Scargle, J.D., 2018. Particle size distributions in chondritic meteorites: evidence for pre-planetesimal histories. Earth Planet Sci. Lett. 494, 69–82. https://doi.org/10.1016/j.epsl.2018.04.021.

Stracke, A., Palme, H., Gellissen, M., Münker, C., Kleine, T., Birbaum, K., Günther, D., Bourdon, B., Zipfel, J., 2012. Refractory element fractionation in the Allende meteorite: implications for solar nebula condensation and the chondritic composition of planetary bodies. Geochem. Cosmochim. Acta 85, 114–141. https://doi.org/10.1016/j.gca.2012.02.006.

Sysoev, A.A., Karpov, A.V., Milyaeva, V.V., Sysoev, A.A., 2018. Novel approach to constructing laser ionization elemental time- of-flight mass spectrometer. Eur. J. Mass Spectrom. 24 (1), 96–107. https://doi.org/10.1177/1469066717743044.

Takayama, A., Tomeoka, K., 2012. Fine-grained rims surrounding chondrules in the Tagish Lake carbonaceous chondrite: verification of their formation through parent-body processes. Geochem. Cosmochim. Acta 98, 1–18. https://doi.org/10.1016/j.gca.2012.08.015.

Tanaka, H., Akai, J., 1997. TEM observation of void-like defect structures in matrix- and isolated-olivine grains in Allende. Antarct. Meteor. Res. 10, 217–226.

Toriumi, M., 1989. Grain size distribution of the matrix in the Allende chondrite. Earth Planet Sci. Lett. 92, 265–273. https://doi.org/10.1016/0012-821X(89)90051-4.

Tulej, M., Riedo, A., Iakovleva, M., Wurz, P., 2012. On applicability of a miniaturized laser ablation time of flight mass spectrometer for trace elements measurements. Int. J. Spectrosc. 14. https://doi.org/10.1155/2012/234949. ID 234949.

Tulej, M., Riedo, A., Neuland, M.B., Meyer, S., Wurz, P., Thomas, N., Grimaudo, V., Moreno-García, P., Broekmann, P., Neubeck, A., Ivarsson, M., 2014. CAMAM: a miniature laser ablation ionisation mass spectrometer and microscope- camera system for in situ investigation of the composition and morphology of extraterrestrial materials. Geostand. Geoanal. Res. 38 (4), 441–466. https://doi.org/10.1111/j.1751-908X.2014.00302.x.

Tulej, M., Neubeck, A., Ivarsson, M., Riedo, A., Neuland, M.B., Meyer, S., Wurz, P., 2015. Composition of micrometer-sized filaments in an aragonite host by a miniature laser ablation/ionization mass spectrometer. Astrobiology 15 (8), 669–682. https://doi.org/10.1089/ast.2015.1304.

Wänke, H., Baddenhausen, H., Palme, H., Spettel, B., 1974. On the chemistry of the Allende inclusions and their origin as high temperature chondensate, Earth and Planet. Sci. Lett. 23 (1), 1–7. https://doi.org/10.1016/0012-821X(74)90022-3.

Wark, D.A., 1979. Birth of the presolar nebula: the sequence of condensation revealed in the Allende meteorite. Astrophys. Space Sci. 65, 275–295. https://doi.org/10.1007/BF00648496.

Watt, L.E., Bland, P.A., Prior, D.J., Russell, S.S., 2006. Fabric analysis of Allende matrix using EBSD. Meteoritics Planet Sci. 41, 989–1001. https://doi.org/10.1111/j.1945-5100.2006.tb00499.x.

Wurz, P., Tulej, M., Riedo, A., Grimaudo, V., Lukmanov, R., Thomas, N., 2021. Investigation of the Surface Composition by Laser Ablation Mass Spectrometry. IEEE Aerospace Conference Big Sjy, MT, USA (in press).

Zhang, B., Miaohong, H., Hang, W., Huang, B., 2013. Minimizing matrix effect by femtosecond laser ablation and ionization in elemental determination. Anal. Chem. 85, 4507–4511. https://doi.org/10.1021/ac400072j.

Zhang, S., Zhang, B., Hang, W., Huang, B., 2015. Chemometrics and theoretical approaches for evaluation of matrix effect in laser ablation and ionization of metal samples. Spectrochim. Acta B. 107, 17–24. https://doi.org/10.1016/j.sab.2015.02.009.

Zolensky, M., Barett, R., Browning, L., 1993. Mineralogy and composition of matrix and chondrule rims in carbonaceous chondrites. Geochem. Cosmochim. Acta 57, 3123–3148. https://doi.org/10.1016/0016-7037(93)90298-B.